

High-energy electron observations by PPB-BETS flight in Antarctica

S.Torii ^a, T.Yamagami ^b, T.Tamura ^c, K.Yoshida ^d, H.Kitamura ^e,
K.Anraku ^c, J.Chang ^f, M.Ejiri ^g, I.Iijima ^b, A.Kadokura ^g,
K.Kasahara ^a, Y.Katayose ^h, T.Kobayashi ⁱ, Y.Komori ^j,
Y.Matsuzaka ^b, K.Mizutani ^k, H.Murakami ^l, M.Namiki ^b,
J.Nishimura ^b, S.Ohta ^b, Y.Saito ^b, M.Shibata ^h, N.Tateyama ^c,
H.Yamagishi ^g, T.Yamashita ^c, T.Yuda ^c

^a*Research Institute for Science and Engineering, Waseda University, 3-4-1 Okubo,
Shinjuku-ku, Tokyo 169-8555, Japan*

^b*Institute of Space and Astronautical Science, JAXA, 3-1-1 Yoshinodai,
Sagamihara 229-8510, Japan*

^c*Institute of Physics, Kanagawa University, 3-27-1 Rokkakubashi, Kanagawa-ku,
Yokohama 221-8686, Japan*

^d*Department of Electronic Information Systems, Shibaura Institute of Technology,
307 Fukasaku, Minuma-ku, Saitama-shi 337-8570, Japan*

^e*National Institute of Radiological Sciences, 4-9-1 Anagawa, Inage-ku, Chiba-shi
263-8555, Japan*

^f*Purple Mountain Observatory, Chinese Academy of Sciences, 2 West Beijing
Road, Nanjing 210008, China*

^g*National Institute of Polar Research, 1-9-10 Kaga, Itabashi-ku, Tokyo 173-8515,
Japan*

^h*Department of Physics, Yokohama National University, 79-1 Tokiwadai,
Hodogaya-ku, Yokohama 240-8501, Japan*

ⁱ*Department of Physics and Mathematics, Aoyama Gakuin University, 5-10-1
Fuchinobe, Sagamihara 229-8558, Japan*

^j*Kanagawa University of Human Services, 1-10-1 Heiseicho, Yokosuka 238-8522,
Japan*

^k*Department of Physics, Saitama University, 255 Shimo-Okubo, Sakura-ku,
Saitama-shi 338-8570, Japan*

^l*Department of Physics, Rikkyo University, 3-34-1 Nishi-Ikebukuro, Toshima-ku,
Tokyo 171-8501, Japan*

Abstract

We have observed cosmic-ray electrons from 10 GeV to 800 GeV by a long duration balloon flight using Polar Patrol Balloon (PPB) in Antarctica. The observation was carried out for 13 days at an average altitude of 35 km in January 2004. The detector is an imaging calorimeter composed of scintillating-fiber belts and plastic scintillators inserted between lead plates with 9 radiation lengths. The performance of the detector has been confirmed by the CERN-SPS beam test and also investigated by Monte-Carlo simulations. New telemetry system using a commercial satellite of Iridium, power supply by solar batteries, and automatic level control using CPU have successfully been developed and operated during the flight. From the long duration balloon observations, we derived the energy spectrum of cosmic-ray electrons in the energy range from 100 GeV to 800 GeV. In addition, for the first time we derived the electron arrival directions above 100 GeV, which is consistent with the isotropic distribution.

Key words: Long duration balloon, Cosmic-ray electrons, Cosmic-ray origin

1 Introduction

High-energy cosmic-ray electrons cannot propagate far from the sources, because the electrons lose rapidly energy with an energy loss rate of the square of energy through the synchrotron and inverse Compton process. Kobayashi et al. (2004) [1] suggests that the energy spectrum of cosmic-ray electrons might have a structure in the energy region over several 100GeV due to the discrete effect of local sources. This means that we can identify cosmic-ray electron sources from the electron spectrum over several 100GeV together with anisotropies in arrival direction. In addition, there is a possibility that Weakly Interacting Massive Particles (WIMPs) annihilate directly into electron-positron pairs and produce mono-energetic electrons and positrons [2]. Although the propagation through the Galaxy would broaden the line spectrum, the observed electron and positron spectrum could still have a distinctive feature. Since there are no other known production mechanisms that would produce an electron and positron peak at energies of 100 GeV - 10 TeV, such a distinctive feature clearly indicates the existence of WIMP dark matter in the Galactic halo. Thus, the observations of high-energy electrons bring us unique information about sources and propagation of cosmic rays, and enable us to search for WIMP dark matter.

Although the cosmic-ray electrons have been observed with many kinds of detectors borne on balloons, most observations are limited below ~ 100 GeV. As an exceptional instance, the observation with the emulsion chambers (ECC) has achieved to detect electrons beyond 1TeV by the large amount of exposures of ~ 14 days in total for 30 years [3,4]. The difficulty of observation originates from that the electron flux itself is very small and decreases with energy much

more rapidly than that of protons because of the electro-magnetic energy loss by radiation. The electron flux is estimated to be $\sim 1\%$ of protons around 10 GeV and less than $\sim 0.2\%$ of protons above 100 GeV from the observed energy spectra with a power-law index of $-3.0 \sim -3.3$ for electrons [6,4] and -2.7 for protons [5]. Therefore, for the electron observations above 100 GeV, we need a long duration observation by a detector with an excellent capability of large geometrical factor and powerful background rejection.

In order to meet the requirements for the electron observation, we have developed a highly granulated imaging calorimeter, the Balloon-borne Electron Telescope with Scintillating fibers (BETS), that preserves the superior qualities of both electronic detectors and emulsion chambers. We have successfully observed cosmic-ray electrons in the energy range from 10 to 100 GeV at Sanriku in Japan [6]. The BETS was improved to observe atmospheric gamma rays at mountain and balloon altitudes for calibrating the atmospheric neutrino flux calculations [7]. Furthermore, for observing the electrons over 100 GeV by a long duration balloon experiment, we have achieved the development of an advanced detector, PPB-BETS, flown by PPB in Antarctica. The PPB has a capability to realize a flight for 2 – 4 weeks in one round of the Antarctica at an altitude of ~ 35 km. The PPB project is carried out by the inter-university collaboration with Institute of Space and Astronautical Science (ISAS), JAXA and National Institute of Polar Research (NIPR) [8,9].

In this paper, we describe the instrumentation of PPB-BETS, the calibration of the detector with accelerator beams, the observations in Antarctica, and the results of our experiments.

2 Instrumentation

2.1 Detector

The PPB-BETS detector consists of 36 scintillating fiber belts, 9 plastic scintillators, and 14 lead plates with 9 radiation lengths (r.l.) in total. Each fiber belt is composed of 280 fibers with a 1mm square cross section for each. A schematic cross section of the detector is shown in Fig. 1. The area of the detector is 28 cm \times 28 cm and the total thickness is 23cm, including spacers inserted between sensitive layers. The scintillating fibers perform the function to detect the shower particles developing in lead plates and to fulfill a detailed imaging of the shower. Scintillating fiber belts are set in right angle alternately to observe the projected shower profile in x and y directions. For the read-out of scintillation light in the fibers, we used an image-intensified CCD camera in each direction of x and y. The plastic scintillators were adopted for the instru-

ment trigger and the energy measurement. Thus PPB-BETS is an instrument to observe the details of three dimensional shower development with a timing capability.

The basic structure of PPB-BETS is similar to the BETS [10]. In order to achieve the observation of electrons up to 1TeV by using a long duration flight, however, the PPB-BETS has been improved in comparison with the BETS at several points presented in the following. The thickness of lead is increased from 7 to 9 r.l. to observe higher energy electrons, and the number of plastic scintillators is increased from 3 to 9 to detect accurately the shower development. The image-intensified CCD camera (I.I.-CCD) system for the read-out of scintillating fibers has newly been developed by using a better quality of CCD to detect 1TeV electron showers without saturation of CCD signals at higher intensities of photon numbers.

The total performance of detector was approved by the beam test using accelerators and by the Monte-Carlo simulations. Monte-Carlo simulations were carried out with several codes such as FLUKA2002 [11,12], GEANT3 [13], and EPICS [14], in which we could not find serious differences.

2.2 Trigger system

The trigger rate in actual observation is critically important to know the data amount transmitted by telemetry, since we have no guarantee of the recovery of instrument. Therefore, we carried out a test flight of the trigger system at Sanriku in advance of the flight in Antarctica. The trigger system is composed of the plastic scintillators and lead plates in same configuration of the PPB-BETS. The flight has confirmed that the trigger system worked well and the rate observed was consistent with the expectation by the simulation. We made also a study on the detailed performance of detector at CERN-SPS by using the electron beams from 10GeV to 200GeV and proton beams from 150 to 350GeV. The electron events developed purely in electro-magnetic process have similar and smooth shower developments. On the other hand, the proton events caused by nuclear interactions have the developments with much wider fluctuations and relatively smaller energy depositions. The detection efficiency of the shower trigger system was examined by adjusting the discrimination levels at each scintillator.

2.3 Imaging system

For the image-intensified CCD camera, it is required to observe shower images from a single track to a shower maximum without saturation. The CCD (THX

7887A) has 1024×1024 pixels, and the signal-to-noise ratio is 70dB that means 6.3 times larger dynamic range of CCD than the BETS of 54dB. Since the pixel number increases by 16 times comparing to that used in BETS, the dynamic range of CCD for the photon intensity in one fiber extends by two order of magnitude. Extrapolating the data of the CERN beam test to higher energies, we confirmed that the I.I.-CCD system has an enough dynamic range for the observation of one single track to 1TeV electrons with linearity. The one CCD image is read out with a speed of 1/30sec by using 12 bit ADC of 40MHz. Pile-up of events in CCD are taken place only by successive events within the timing of $10\mu\text{sec}$, and the effect can be negligible small. The total data processing on-board take $\sim 1\text{sec}$ for one event.

Since the instrument is not scheduled to be recovered, all of the observed data should be transferred by the Iridium satellite phone line and the down link to the Syowa station. To meet the telemetry rate of 2.4kbps by Iridium, the image data can be compressed on-board with a Run-Length method and a Huffman method. From the beam test, we obtained that the compressed image data size of one event is $\sim 18\text{kByte}$ for electrons at 100 GeV and $\sim 13\text{kByte}$ for protons at 100 GeV with the data compression rate of $\sim 40\%$.

2.4 Ballooning technology

As a ballooning technology of the long duration flight, we have developed the telemetry system with the Iridium satellite phone system, power supply system by solar batteries, automatic level control system using CPU, and so on. Since the detector weight should be saved for loading the heavy ballast, we used an un-pressurized vessel with a light shield, designing the instrument to meet the vacuum and heat conditions during the long duration flight. We examined the validity of the instrument by environmental tests as long as more than one week.

We summarize the basic parameters of the PPB-BETS instrument in Table 1.

3 Observations

The balloon was launched at the Syowa station ($69^{\circ}00'$ latitude south, $35^{\circ}35'$ longitude east) in Antarctica at 15:57 on January 4, 2004 (UTC). The level flight was started at 18:00 on January 4, and continued till 1:46 on January 17, 2004 (UTC) at altitudes of 33-37 km (35km on average). The total duration of the exposure time is 2.96×10^2 hr. The trajectory of the PPB-BETS is presented in Fig. 2. The balloon went round the Antarctica at $\sim 65^{\circ}$ latitude

south from east to west with a speed of $\sim 30 - 35 \text{ km h}^{-1}$. Power consumption of 70W in the instrument was normally supplied by the solar batteries. Automatic level control system successfully operated as presented in Fig. 3.

The event trigger was executed by two modes, the high-energy (HE) mode and low-energy (LE) mode. The LE mode corresponds to electron observation over 10GeV, and was assigned for the observation during 10 hours just after launching. The data acquired by the LE mode were directly transferred to the Syowa station with a telemetry of 64kbps. The HE mode, which corresponds to the electron observation over 100GeV, was used through all the flight. The acquired data were further selected by the software trigger (2nd trigger) on-board, and transmitted to our operation room at NIPR in Japan, via a receiving station in US, with an Iridium satellite phone line at a rate of 2.4kbps. The commands from the operation room to the PPB-BETS were also sent by the Iridium line. The monitoring data were delivered to each institute via Internet. The data transfer rates were $\sim 1 \times 10^4$ events per hour (3Hz) for the LE mode and ~ 70 events per hour (0.02Hz) for the HE mode, respectively. The amount of data used for the current analysis is $\sim 1/4$ of the acquired data on-board because of the problem of data transfer system and CCD noise.

4 Data analysis

4.1 Data sets for analysis

For the event triggering the HE mode, we adopted two main sets of discrimination levels of pulse heights in all these plastic scintillators. One set corresponds to the threshold energy of 100 GeV and the other to 150 GeV. The number of acquired events is 3.1×10^3 for the 100 GeV threshold and 1.6×10^3 for the 150 GeV threshold. There are also 1.0×10^3 events for the other thresholds on the HE mode. In this analysis, we used the two data sets of the 100 GeV and 150 GeV threshold without use of the other data including the LE mode. Figure 4 shows the pulse height (converted to the number of Minimum Ionizing Particle, MIP) distribution of the plastic scintillator at the depth of 7 r.l. for the two thresholds. As shown in Fig. 4, the observable minimum energy is shifted properly depending on each threshold, and the trigger system worked normally. The spectra in high-energy region are compared to a power-law spectrum with an index of -2.7 . They are consistent with the spectral shape of the cosmic-ray protons, since the events triggered on-board are still dominated by the protons that are much more abundant than the electrons.

4.2 Energy measurement

The plastic scintillators are used for the energy measurements of electrons. Since the number of shower particles at the shower maximum is nearly proportional to the energy of incident electrons, we determined the electron energies by using the number of particles at the shower maximum in the transition curve with plastic scintillators. The transition curves of electro-magnetic shower are well represented by the following formula:

$$S = N\left(\frac{bt}{\cos\theta}\right)^{a-1}\exp\left(-\frac{bt}{\cos\theta}\right), \quad (1)$$

where S is the pulse heights (converted to MIP) of plastic scintillators at the depth of t r.l., N is the normalization factor, θ is the zenith angle of the shower axis, and a and b are adjustable coefficients. In order to derive the number of particles at the shower maximum, we fitted this formula to the pulse heights of the six scintillators at depths of 3 r.l. to 9 r.l. As shown in Fig. 5, the relation of the number of particles at the shower maximum and the energies of electron beams at CERN-SPS is almost linear in the energy range of 10 – 200 GeV. The energy resolution is 12 % at 100 GeV as shown in Fig. 6, and consistent with the simulations.

4.3 Angular measurement

It is important to determine accurately a shower axis, since it is crucial to determine the electron energy and the separation of electrons from background protons and gamma rays as mentioned later.

For the acquired events in the flight, we reconstructed the raw CCD images of showers to the fiber positions in detector space by using the positions of each fiber on the CCD image. The positions of each fiber were obtained in advance of the flight by observing cosmic-ray muon tracks at ground level. The relative displacement of the fiber positions during the flight was calibrated by using the LED-illuminated fibers. Examples of the reconstructed shower image observed in the flight are presented in Fig. 7.

From the reconstructed shower image, we determine the shower axis in the following. At first, below 3 r.l. in the detector, we derive centric positions of shower lateral spreads in each fiber layer. By fitting these centric positions with a linear least-squares method we determine a tentative shower axis, and trace back to the next upper layer. Adding a new centric position in the upper layer by using only fiber signals near the tentative shower axis (± 5 fibers), we fit the shower axis once again. This process is repeated up to the top layer of

0 r.l., and the shower axis is determined. Figure 8 shows the angular resolution by the beam test, which ranges from 0.40 to 0.57 degree with electron energies of 10 to 200 GeV. Although they are considerably better than those of the BETS of $\sim 1^\circ$, they are worse than the simulated angular resolution of $\sim 0.15^\circ$ above 100 GeV. It is caused by errors of the fiber positions in detector space.

4.4 Electron selection

The electron selection from backgrounds has been carried out by the method used in BETS as explained below. At first, proton backgrounds are reduced with the on-board trigger system. The discrimination levels are set with each scintillator. Second, we selected the events whose shower axes pass through the top and bottom of the detector within a zenith angle of 30 degrees. This selection reduces the proton background events triggered on-board, which are incident from the side of the detector. Third, we introduced the ratio of energy deposition within 5mm from the shower axis to the total (RE parameter) as described in Torii et al. (2001) [6]. A typical event of electron-induced shower presents a narrower lateral spread concentrated along the shower axis, as shown in Fig. 7. On the contrary, that of proton-induced shower shows a wider lateral spread. We characterize this physical property by the RE parameter. The electron candidates were selected by the RE distribution under the condition that the RE values are greater than 0.75 [15].

As for the separation between electrons and gamma rays, electrons could be identified by the presence of hits in the scintillating fibers at 0 r.l. along the shower axis. Incident electrons leave signals on the fibers along the shower axis. On the other hand, incident gamma rays leave no signals except for the back-scattered particles. We judged electrons as the events whose distances are less than or equal to 5 mm. Gamma-ray events are rejected by 90 % [15].

As a result, the number of the electron candidates above 100 GeV is 84 events among the 4.7×10^3 analyzed events in the HE mode.

4.5 Derivation of electron energy spectrum

From the electron events, with the above selection and energy determination, we derived the cosmic-ray electron spectrum by using the following formula:

$$J_e(E) = \left(\frac{N_e C_{RE} C_{eg}}{S \Omega T \Delta E} C_{enh} - C_{2nd} \right) C_{atm}, \quad (2)$$

where N_e is the number of electron candidates, $S\Omega$ the effective geometrical factor, T the observed live time, ΔE the energy interval, C_{RE} the correction factor of the proton contamination in the RE -cut with energy dependence, C_{eg} the correction factor of the gamma-ray contamination in the gamma-ray rejection with energy dependence, C_{enh} the correction of enhancement of flux due to the energy resolution, C_{2nd} the flux of secondary (atmospheric) electrons at the observation level, and C_{atm} the correction factor of energy loss of primary electrons in the overlying atmosphere.

The effective geometrical factor, $S\Omega$, is derived by Monte-Carlo simulations under the same condition of the experiment. Figure 9 shows the effective geometrical factor with electron energies for the 100 GeV threshold and 150 GeV threshold in the HE mode.

The uncertainty of the energy determination has the effect of enhancing the absolute flux of electrons, in particular, for a steep power-law spectrum. We derived the enhancement factor C_{enh} above 100 GeV of 0.98 due to the energy resolution presented in Fig. 6.

In order to derive the primary electron spectrum, we subtracted the secondary electrons produced by the interactions of cosmic-ray nuclei. The energy spectrum of the estimated atmospheric electrons are represented by

$$C_{2nd}(E) = 1.32 \times 10^{-5} \left(\frac{E}{100 \text{ GeV}} \right)^{-2.73} (\text{m}^{-2} \text{s}^{-1} \text{sr}^{-1} \text{GeV}^{-1}) \quad (3)$$

at the altitude of 7.4 g cm^{-2} [3,23].

The atmospheric correction factor, C_{atm} , is caused by bremsstrahlung energy losses of the primary electrons. In the case of a single power-law spectrum with an index of $-\gamma$, the energy-loss correction due to the overlying atmosphere is given by $\alpha = e^{A(\gamma-1)t/(\gamma-1)}$, where t is the depth in r.l., and the notation A refers to the formula used in electro-magnetic shower theory [3]. The energy-loss correction, α , corresponds to the correction factor of flux as follows: $C_{atm} = \alpha^{\gamma-1}$. In the case of $\gamma = 3.0$ and 7.4 g cm^{-2} depth, the atmospheric correction factor is $C_{atm} = 1.37$ for $\alpha = 1.17$.

From the raw numbers of electron candidates, we evaluated the electron numbers by correcting the proton contamination in the RE cut and the gamma-ray contamination in the gamma-ray rejection. Since the power-law index of the primary proton spectrum is -2.7 , which is much harder than that of the electrons, the contamination of protons increases with energy. Atmospheric gamma rays are also produced by the interaction of primary protons with atmospheric nuclei. Therefore, the index of gamma rays is the same with that of protons. This brings the same energy dependence for the contamination of gamma rays with the protons. Hence, the correction factors are estimated

to be $C_{\text{RE}} = 1 - 0.325 \times (E/100\text{GeV})^{\gamma-2.7}$ for the proton contamination and $C_{\text{eg}} = 1 - 0.176 \times (E/100\text{GeV})^{\gamma-2.7}$ for the gamma-ray contamination from the Monte-Carlo simulations.

4.6 Check on event identification

In order to check on the event identification, we derived the zenith angle distribution of electron and gamma-ray events. For cosmic-ray electrons, the zenith angle distribution will be isotropic, and thus for a plane detector the observed angular distribution will be proportional to $\cos\theta d(\cos\theta)$, neglecting the effect of the finite detector size. The distribution for atmospheric gamma rays should be constant with $\cos\theta$, since the gamma rays are produced in the overlying residual atmosphere and thus have a $1/\cos\theta$ enhancement relative to the isotropic primary hadron flux. Zenith angle distributions for the electrons and gamma rays are presented in Fig. 10, and in good agreement with the expected forms with the finite detector size.

We also derived the vertical spectrum of atmospheric gamma rays at 7.4 g cm^{-2} originated from hadronic interactions, subtracting the bremsstrahlung gamma rays produced by primary cosmic-ray electrons. Figure 11 shows the observed spectrum of atmospheric gamma rays at 7.4 g cm^{-2} , which is well represented by

$$J_{\gamma} = (3.19 \pm 0.59) \times 10^{-4} \left(\frac{E}{100\text{GeV}} \right)^{-2.77 \pm 0.21} (\text{m}^{-2}\text{s}^{-1}\text{sr}^{-1}\text{GeV}^{-1}). \quad (4)$$

The spectral shape is in good agreement with the ECC and the calculated results from hadronic interactions of primary cosmic rays with the overlying atmosphere [23]. At the normalized depth of 7.4 g cm^{-2} , the gamma-ray flux agrees with the BETS in the energy region of 10 – 20 GeV [7], and is consistent with that of ECC within 95% confidence level of statistical errors.

5 Results and discussions

5.1 Energy spectrum of electrons

Figure 12 presents the electron energy spectrum multiplied by the cube of energy, in comparison with other electron observations [16,17,18,19,6,20,4,21]. Table 2 presents the flux of electrons at the top of atmosphere in each energy interval. Our spectrum agrees well with the extrapolated spectrum of the

BETS[6] at 100 GeV. The combined spectrum of PPB-BETS and BETS can be represented by a single power-law function of

$$J_e = (1.82 \pm 0.13) \times 10^{-4} \left(\frac{E}{100 \text{ GeV}} \right)^{-3.05 \pm 0.05} (\text{m}^{-2} \text{s}^{-1} \text{sr}^{-1} \text{GeV}^{-1}) \quad (5)$$

in the energy range of 10 GeV to 800 GeV. The reduced chi-square value is 1.605 for 11 degrees of freedom. A power-law spectrum is acceptable at the 95 % confidence level of statistical errors.

The energy spectrum exceeding 100 GeV is crucial to detect the nearby SNRs as discussed by Kobayashi et al. (2004) [1], and electron-positron pairs from Kaluza-Klein dark matter annihilations [2]. Although the data statistics of our results are insufficient to discuss the details of the contribution of nearby SNRs and/or WIMP dark matter, our energy spectrum may indicate a sign of a structure in the several 100 GeV region, as shown in Fig. 12. Similar structure in the electron energy spectrum is reported by the ATIC-2 observations [21]. Therefore, although the energy spectrum with PPB-BETS cannot reject a single power-law function, both the observations with PPB-BETS and ATIC-2 may indicate a significant spectral structure. For the future observations, we are planning to increase greatly our statistics by experiments such as CALET with the geometrical factor of nearly $1 \text{ m}^2 \text{sr}$ and the observation time of 3 years on the International Space Station [22]. It is expected that CALET can detect these distinctive signatures from the nearby SNRs and WIMP annihilations [27].

5.2 Arrival directions of electrons

Incident directions of electrons on the PPB-BETS detector are determined by using the shower axis with an accuracy of around 0.5 degree. Since the attitudes of PPB-BETS instrument are determined with sun aspect sensors and geomagnetic aspect sensors, we can determine arrival directions of cosmic-ray electrons with an accuracy of several degree. For the determination of attitudes with geomagnetic aspect sensors, we referred to the International Geomagnetic Reference Field (IGRF) model [24]. From these capabilities of PPB-BETS, for the first time we derived the arrival directions of high-energy electrons. Figure 13 presents a ratio of the observed distribution above ~ 100 GeV to the isotropic distribution along the Galactic longitude. As shown in Fig. 13, the arrival directions of electrons are consistent with the isotropic distribution.

Because the rate of energy loss due to the synchrotron and inverse Compton processes is much higher for electrons than for nuclei, the degree of anisotropy of high-energy cosmic ray electrons is expected to be higher than that of the

nuclear component [25,26]. The magnitude of anisotropy is expected to be only around 1 % in the 100 GeV – 1 TeV in the direction of Vela at $(\ell, b) = (-96^\circ.1, -3^\circ.3)$ by using the calculated results by Kobayoashi et al. (2004) [1,28]. The first result of the electron arrival directions by PPB-BETS shows no significant anisotropy within statistical errors. For the future observations, the detection of anisotropy toward the sources will enable us to identify the cosmic-ray electron sources, together with the unique signatures of the energy spectrum described above.

6 Acknowledgment

The PPB-BETS project was carried out in collaboration with NIPR and ISAS/JAXA. We express special thanks to the members who participated in the PPB-BETS project, including the members in the JARE-44, who carried out the excellent and successful balloon flight at Syowa Station. We also thank the staffs of the H4 beam line of CERN-SPS for their kind support. This work was partly supported by Grants in Aid for Scientific Research on Priority Area A (Grant No.14039212) and Scientific Research C (Grant No.16540268, No.18540293).

References

- [1] Kobayashi,T., Komori,Y., Yoshida,K. et al. *Astrophys. J.* 601, 340-351, 2004.
- [2] Cheng,H.C., Feng,J.L., Matchev,K.T., *Phys. Rev. Lett.* 89, 211301-1-4, 2002.
- [3] Nishimura,J., Fujii,M., Taira,T. et al. *Astrophys. J.* 238, 394-409, 1980.
- [4] Kobayashi,T., Komori,Y., Yoshida,K. et al. *Uchuken Houkoku SP 44*, 99-125, 2002.
- [5] Haino,S., Sanuki,T., Abe,K. et al. *Phys. Lett. B* 594, 35-46, 2004.
- [6] Torii,S., Tamura,T., Tateyama,N. et al. *Astrophys. J.* 559, 973-984, 2001.
- [7] Kasahara,K., Mochizuki,E., Torii,S. et al. *Phys. Rev. D* 66, 052004 (1-9), 2002.
- [8] Nishimura,J., Yajima,N., Akiyama,H. et al. *Jour. Aircraft* 31 (6), 1264-1267, 1994.
- [9] Kadokura,A., Yamagishi,H., Sato,N. et al. *Advances in Polar Upper Atmosphere Physics* 16, 157-172, 2002.
- [10] Torii,S., Tamura,T., Tateyama,N. et al. *Nucl. Instrum. Methods Phys. Res. A* 452, 81-93, 2000.

- [11] Fassò,A., Ferrari,A., Sala,P.R. Proc. MonteCarlo 2000 Conf., 159-164, 2001.
- [12] Fassò,A., Ferrari,A., Ranft,J. et al. Proc. MonteCarlo 2000 Conf., 955-960, 2001.
- [13] Apostolakis,J. <http://www.asd.web.cern.ch/wwwasd/geant/>, 2003.
- [14] Kasahara,K. <http://eweb.n.kanagawa-u.ac.jp/~kasahara/ResearchHome/EPICSHome/>, 2003.
- [15] Yoshida,K., Torii,S., Yamagami,T. et al. Adv. Space Res. 42, in press, 2008.
- [16] Tang,K.K., Astrophys. J. 278, 881-892, 1984.
- [17] Golden,R.L., Mauger,B.G., Badhwar,G.D. et al., Astrophys. J. 287, 622-632, 1984.
- [18] Boezio,M., Carlson,P., Francke,T. et al., Astrophys. J. 532, 653-669, 2000.
- [19] DuVernois,M.A., Barwick,S.W., Beatty,J.J. et al., Astrophys. J. 559, 296-303, 2001.
- [20] Aguilar,M., Alcaraz,J., Allaby,J. et al., Physics Reports 366, 331-405, 2002.
- [21] Chang,J., Schmidt,W.K.H., Adams,J.H. et al. Proc. of 29th ICRC (Pune) 3, 1-4, 2005.
- [22] Torii,S. et al. Nucl. Phys. B (Proc. Suppl.) 150, 345-348, 2006.
- [23] Yoshida,K., Ohmori,R., Kobayashi,T. et al. Phys. Rev. D 74, 083511-1-13, 2006.
- [24] WDC for Solid Earth and Geophysics, <http://www.ngdc.noaa.gov/IAGA/vmod/igrf.html>, 2005.
- [25] Shen,C.S. & Mao,C.Y., Astrophys. Lett. 9, 169-174, 1971.
- [26] Ptuskin,V.S. & Ormes,J.F., Proc. of 24th ICRC (Roma) 3, 56-59, 1995.
- [27] Torii,S., Yoshida,K., Kasahara,K. et al. Adv. Space Res. 41, 2032-2036, 2008.
- [28] Yoshida,K., Adv. Space Res. 42, 477-485, 2008.

Table 1
Basic parameters of the PPB-BETS

Instrument weight	200 kg	including un-pressurized gondola
(Total weight	480 kg	including ballast)
Power consumption	70 W	supplied by solar batteries
Level altitude	~35 km	by automatic level control
Data transfer rate	2.4 kbps	by the Iridium phone line
	64 kbps	by the down link to the station
Energy range	10 GeV–1 TeV	by two trigger modes
Effective geometrical factor	~300 cm ² sr	> 100 GeV by simulation
Energy resolution	10-20 %	in 10 GeV–1 TeV by plastic scintillators
Angular resolution	0.4–0.6 deg	by scintillating fibers

Table 2
Electron flux at the top of atmosphere

E (GeV)	\bar{E} (GeV)	Intensity ^a (m ⁻² s ⁻¹ sr ⁻¹ GeV ⁻¹)
100.0–158.5	122.6	$(8.1 \pm 1.6) \times 10^{-5}$
158.5–251.2	194.4	$(3.4 \pm 0.7) \times 10^{-5}$
251.2–398.1	308.0	$(9.0 \pm 2.4) \times 10^{-6}$
398.1–631.0	488.2	$(2.8 \pm 0.8) \times 10^{-6}$
631.0–1000.0	773.7	$(2.0 \pm 0.9) \times 10^{-7}$

^a The quoted errors are the statistical error.

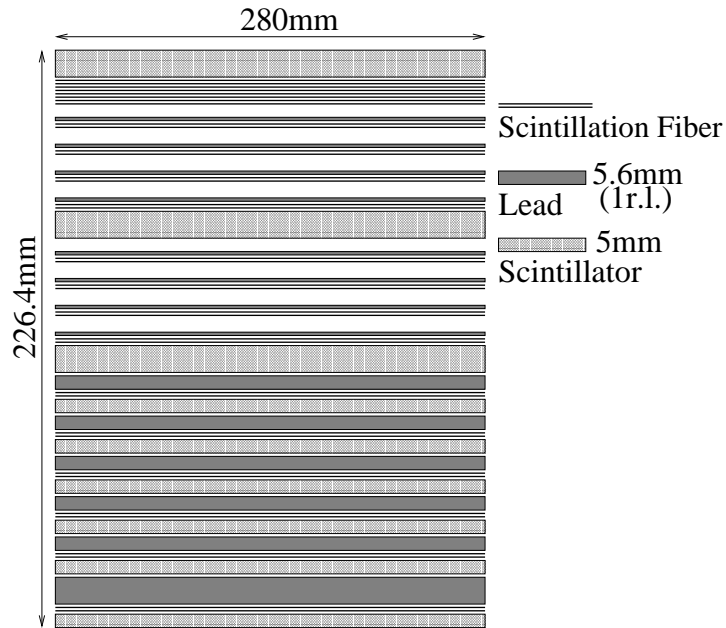


Fig. 1. Schematic side view of the PPB-BETS detector. See text for details.

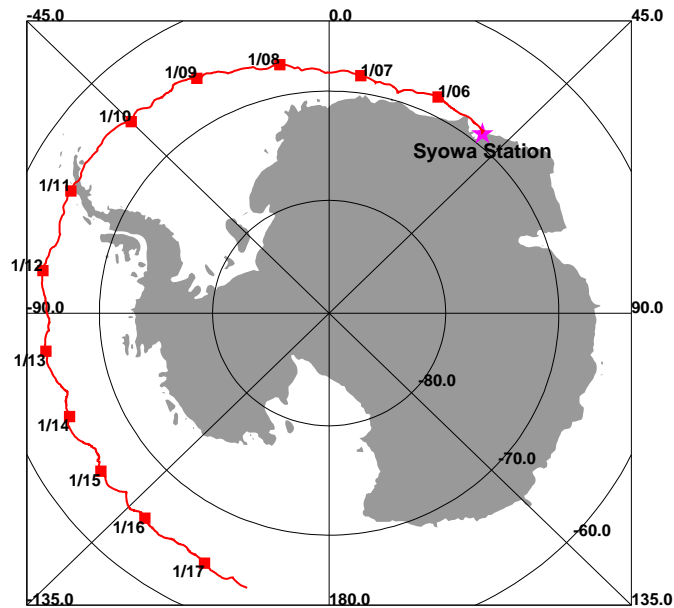


Fig. 2. The trajectory of the PPB-BETS in Antarctica.

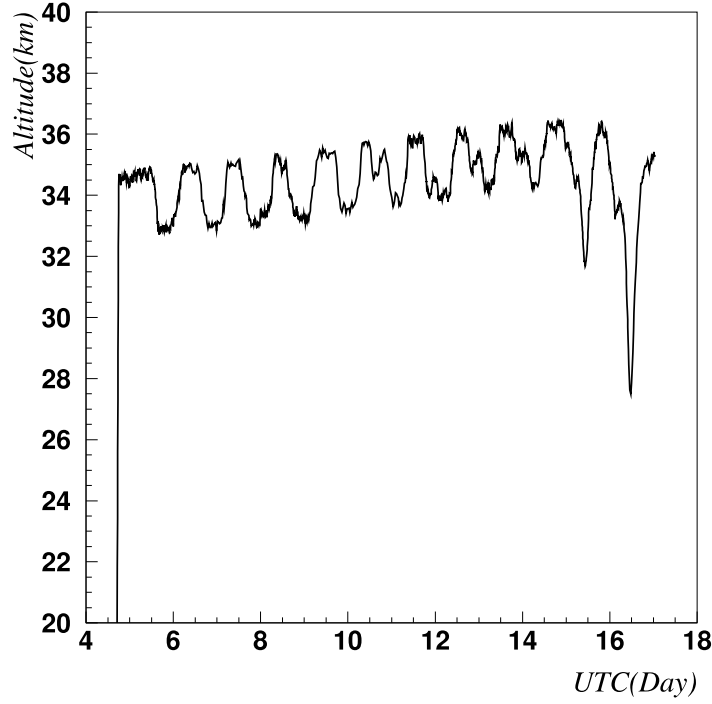


Fig. 3. The altitude profile of the PPB-BETS.

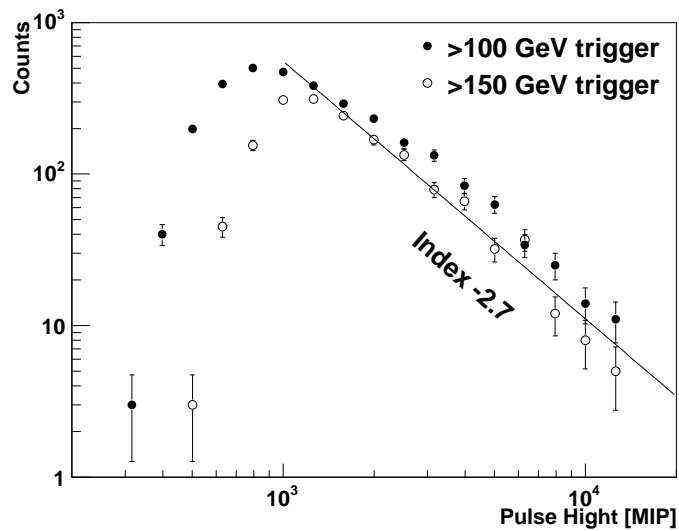


Fig. 4. Pulse height distributions of the plastic scintillator at the depth of 7 r.l. for the 100 GeV threshold (solid circles) and 150 GeV threshold (open circles). The solid line shows a power-law spectrum with an index of -2.7 .

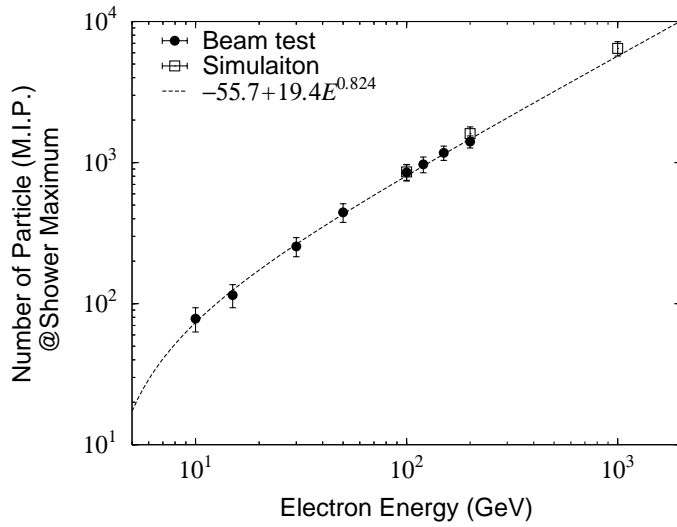


Fig. 5. Relation of the electron energy and the number of shower particles at the shower maximum by the CERN-SPS beam tests with simulations. The incident direction is perpendicular to the detector surface.

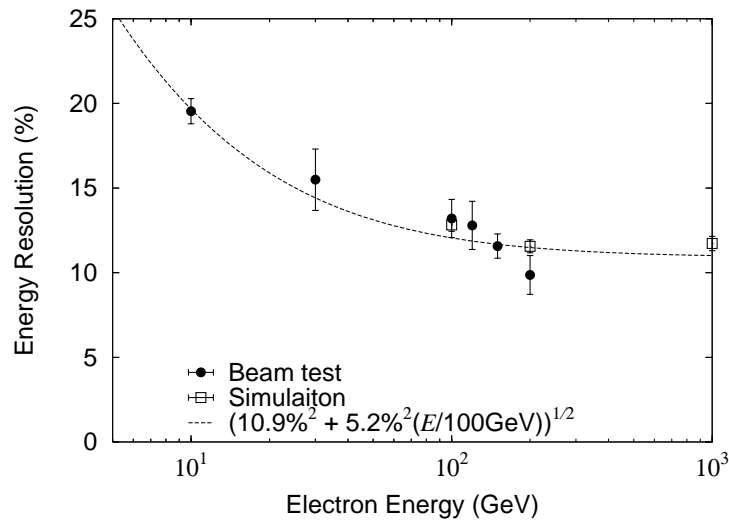


Fig. 6. Energy dependence of the energy resolution for the CERN-SPS electron beams with simulations. The incident direction is perpendicular to the detector surface.

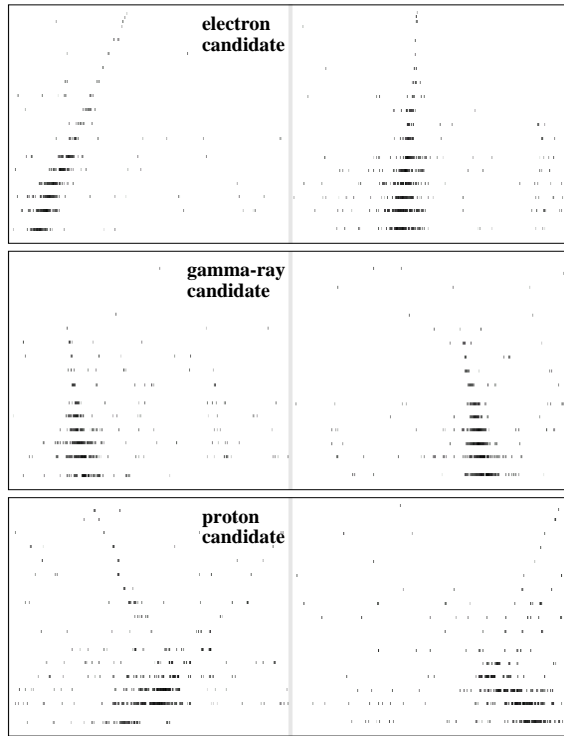


Fig. 7. Examples of the reconstructed images in detector space. Typical candidates of an electron, gamma ray, and proton are shown in x and y directions.

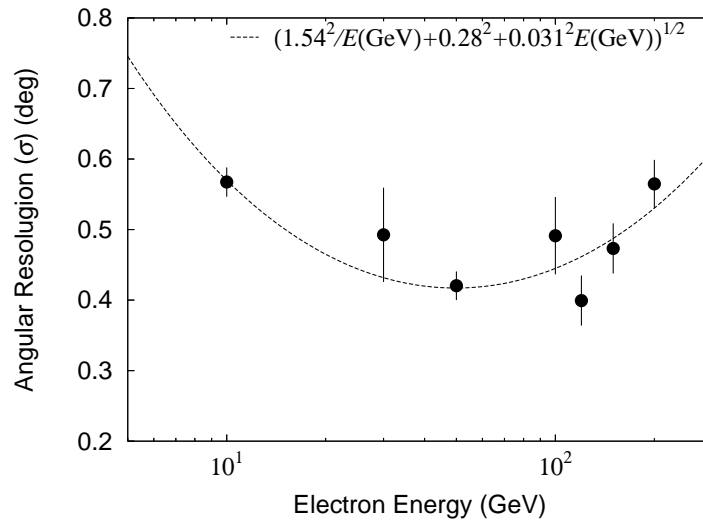


Fig. 8. Energy dependence of the angular resolution for the perpendicular electron beams at CERN-SPS.

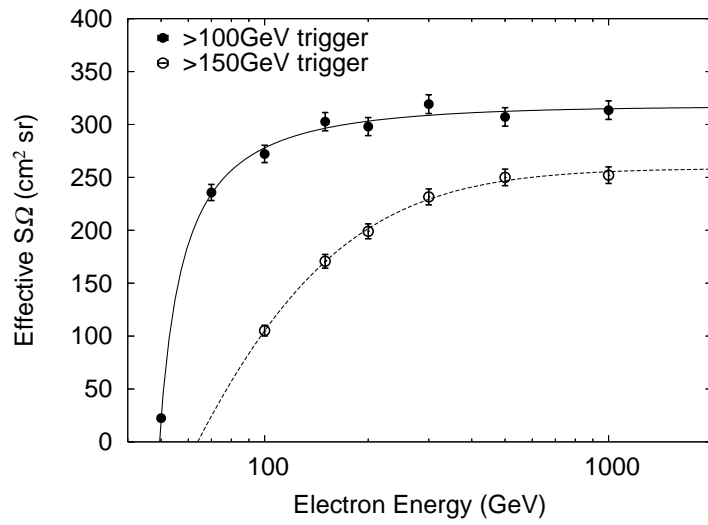


Fig. 9. The effective geometrical factor $S\Omega$ with the Monte-Carlo simulations under the same condition of the experiment.

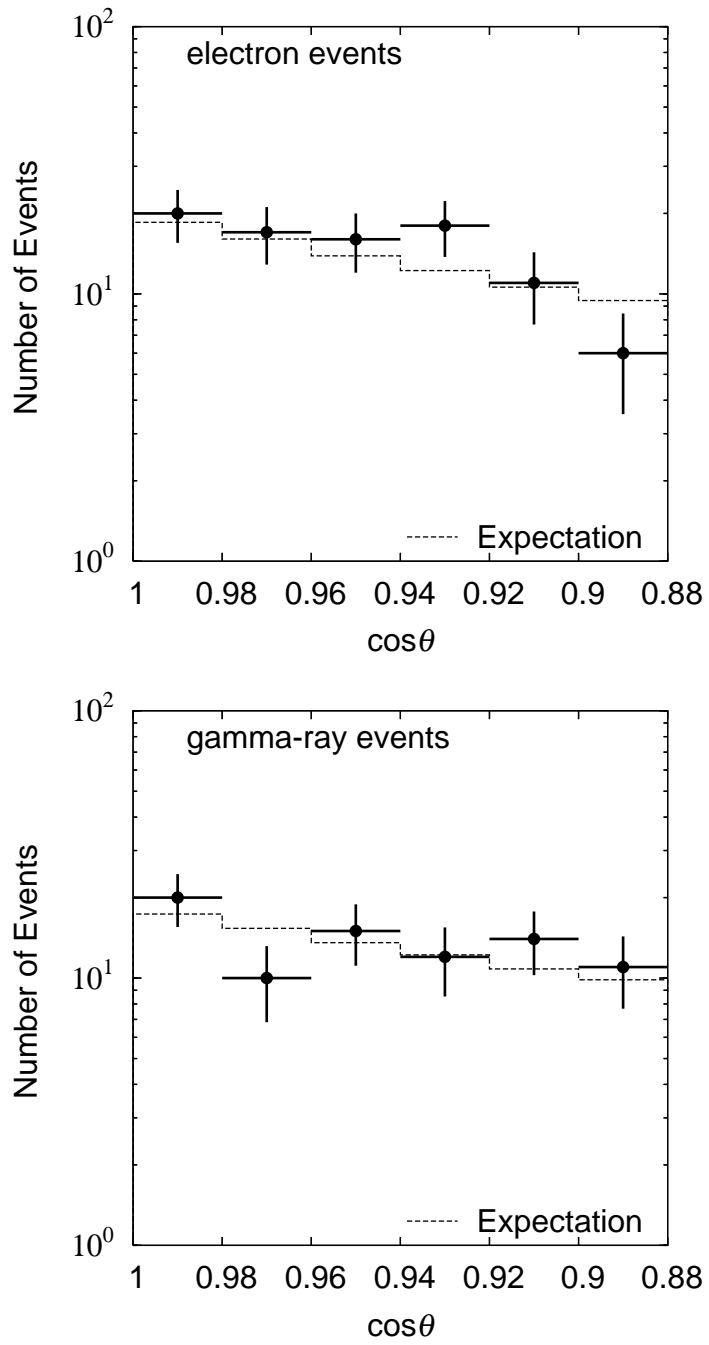


Fig. 10. Zenith angle distributions for events classified as electrons and gamma rays with the expected distributions.

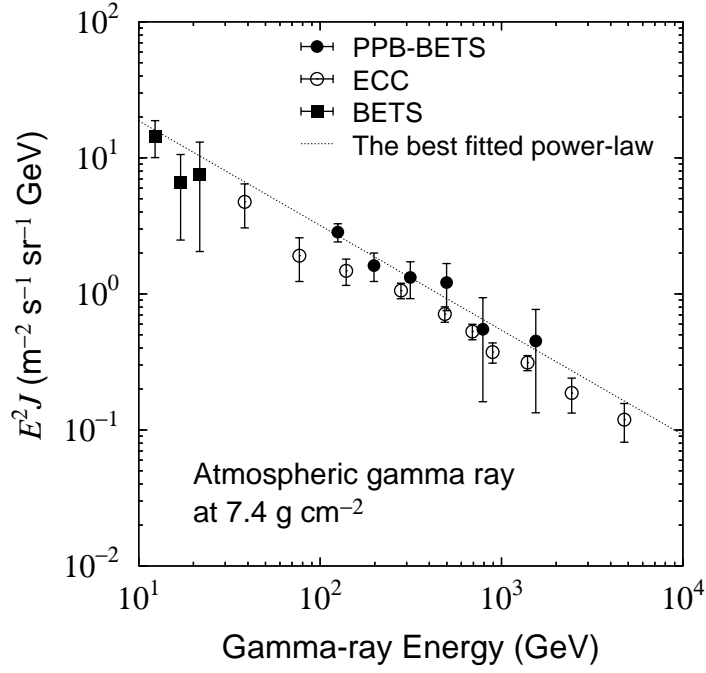


Fig. 11. Energy spectrum of atmospheric gamma rays observed with PPB-BETS, compared to the BETS [7] and ECC [23]. The gamma-ray fluxes are normalized to 7.4 g cm^{-2} equivalent altitude. The dash line shows the best fit power-law function of PPB-BETS data with an index of -2.77 ± 0.21 .

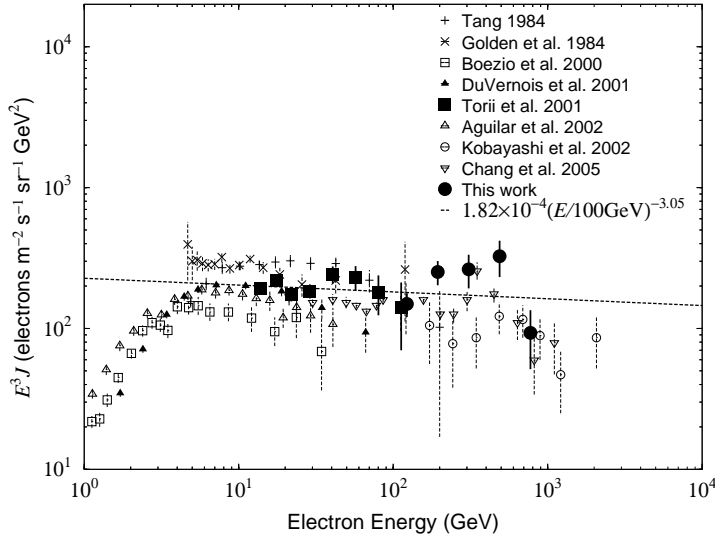


Fig. 12. Electron energy spectrum observed with PPB-BETS (solid circles) in comparison with the energy spectra of BETS (solid squares) and the other observations. The dash line shows the best fit power-law function of the combined spectrum of PPB-BETS and BETS with an index of -3.05 ± 0.05 .

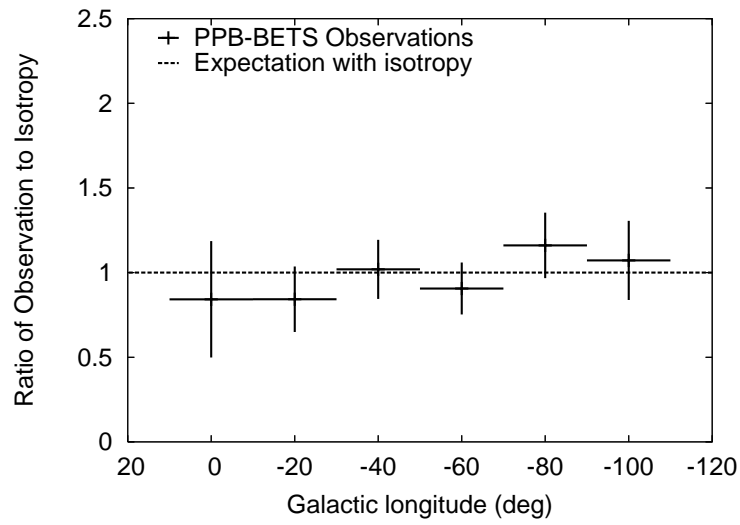


Fig. 13. A ratio of the electron flux observed with PPB-BETS to the isotropic distribution along the Galactic longitude.